Interplay of Pd ensemble sites induced by GaO_x modification in boosting CO_2 hydrogenation to formic acid

Kohsuke Mori [a,b,*], Hiroto Hata [a], Hiromi Yamashita [a,b,*]

[a] *Division of Materials and Manufacturing Science, Graduate School of Engineering, Osaka University, 2-1 Yamada-oka, Osaka 565-0871, Japan*
[b] *Innovative Catalysis Science Division, Institute for Open and Transdisciplinary Research Initiatives (ICS-OTRI), Osaka University, Suita, Osaka 565-0871, Japan*

A B S T R A C T

The interfacial modification of Pd nanoparticles supported on g-C_3N_4 (CN) was performed using highly dispersed amorphous MO_x phase, where M represents Ga, Al, or B. The resulting $Pd@MO_x$/CN exhibited enhanced activity in the hydrogenation of CO_2 to yield formic acid. In particular, $Pd@GaO_x$/CN displayed a maximum turnover number of 4540 based on the quantity of surface-exposed Pd atoms; this turnover number is more than six times higher than that of the unmodified catalyst. DFT calculations show that the presence of GaO_x clusters on the Pd (111) surface produces the unique Pd ensemble sites, where electron-deficient $Pd^{\delta+}$ and electron-rich $Pd^{\delta-}$ are adjacent. On the basis of kinetic and theoretical investigations, we propose a reasonable dual activation mechanism: the electron-deficient $Pd^{\delta+}$ species facilitates the adsorption of HCO_3^- ions, whereas the electron-rich $Pd^{\delta-}$ species accelerates not only H_2 dissociation but also the attack of dissociated H atoms on C atoms in HCO_3^- ions.

1. Introduction

The hydrogenation of CO_2 to formic acid (FA; HCOOH) is of significant interest not only because CO_2 is an inexpensive, nontoxic, abundant C1 feedstock but also because FA is considered to be a renewable hydrogen storage material due to its relatively high hydrogen content (53 $g \cdot L^{-1}$), low toxicity, and nonflammable characteristics [1–5]. The gas-phase hydrogenation of CO_2 to produce FA has a positive free energy change ($\Delta G = +33$ $kJ \cdot mol^{-1}$) [6], but this reaction proceeds more readily in aqueous solution ($\Delta G = -4$ $kJ \cdot mol^{-1}$) [7]. This reaction is typically performed with the addition of a weak base (B), which shifts the thermodynamic equilibrium to the product side: CO_2 (aq) + H_2 (aq) + B → HCO_2^- (aq) + BH^+, $\Delta G = -35.4$ $kJ \cdot mol^{-1}$ [8]. Significant efforts have been devoted to the research of homogeneous transition metal complexes in basic media, and some of these catalytic systems have proven extremely efficient [9–11]. Unfortunately, advancements in reliable heterogeneous catalysts for FA synthesis via CO_2 hydrogenation have lagged behind [5,12–14].

We previously investigated a series of supported PdAg nanoparticle (NP) catalysts, such as random PdAg, Pd@Ag, and Ag@Pd, on TiO_2 prepared using surface engineering approaches with atomic precision [15]. A strong correlation has been demonstrated between increased

catalytic activity and increased electron negativity of active Pd atoms due to a synergy between effects originating from Pd and Ag. Kinetic and density functional theory (DFT) calculations demonstrated that this synergistic effect boosts the attack on the C atom in adsorbed HCO_3^- at a positively charged Ag site by a dissociated H atom at a negatively charged Pd site. These results provide advanced insight into a possible design strategy for catalytically active sites for CO_2 hydrogenation to FA [16].

In nano-engineering, an ongoing challenge in the field of catalyst design, the angstrom-scale and nanoscale architecture of NPs plays a dominant role in determining their efficiency and selectivity [17–19]. Control of particle size is essentially utilized to tune the concentration of low-coordination sites and surface vacancies, allowing effective utilization of expensive catalyst metals [20–22]. Special nanostructures such as rods, cubes, and polycrystals are known to exert a strong influence on catalytic activity and selectivity due to differences in the preferential exposure of particular crystallographic planes.[23–25] The utilization of the strong metal–support interaction between metal NPs and catalyst supports frequently leads to unique synergestic effects at their interfaces, which further influence particle size and the overall size distribution of metal NPs [26–28] Surface modification with organic ligands not only inhibits the aggregation of metal NPs but also controls

---

the adsorption kinetics of reactants or intermediates through specific geometric effects or metal–ligand electronic effects [29–32]. In alloys with second and third metals, the coordination of one metal to another can provide novel active sites and often alters electronic properties, endowing catalytic activity and selectivity superior to those of monometallic counterparts [33–36].

In this study, we utilized highly dispersed MO_x phase (where M represents a group 13 element, namely, Ga, Al, or B) as inorganic ligands to alter the electronic state of surface Pd NPs, with the aim of improving catalytic performance during CO_2 hydrogenation to produce FA. Unlike organic ligands, which exhibit Lewis basicity, the oxide (O_2^-) moieties of MO_x ligands connect with metal centers to form extended structures. In these structures, specific group 13 metal ions influence its coordinating ability and ultimately determine catalytic performance. Modification with GaO_x produced a maximum turnover number based on the quantity of surface exposed Pd atoms, which is six times higher that of the unmodified Pd catalyst. Such enhancement is attributed to the interplay of unique Pd ensemble sites with the aid of associated MO_x ligands. In this interplay, the electron-deficient $Pd^{\delta+}$ species facilitates the adsorption of HCO_3^- ions, whereas the electron-rich $Pd^{\delta-}$ species accelerates not only H_2 dissociation but also the attack of dissociated H atoms on C atoms in HCO_3^- ions, as evidenced by kinetic and DFT calculations.

2. Experimental section

2.1. Materials

Na_2PdCl_4 was obtained from Tokyo Kasei Kogyo Co., Ltd. Melamine, $Ga(NO_3)_3 \cdot nH_2O$, and $Al(NO_3)_30.9\ H_2O$ were purchased from Nacalai Tesque. H_3BO_3 and $NaHCO_3$ were purchased from Wako Pure Chemical Industries, Ltd. All commercially available compounds were used as received. Distilled water was employed as the reaction solvent.

2.2. Synthesis of GaO_x-modified Pd/g-C_3N_4 (Pd@GaO_x/CN)

g-C_3N_4 was prepared according to a previously reported procedure [37]. Melamine of 30 g was heated in a muffle furnace in air at 550 °C for 4 h to give a yellow solid. The solid was crushed into powder in a mortar. The obtained g-C_3N_4 (0.5 g) was dispersed in 100 mL of an aqueous solution containing Na_2PdCl_4 (0.047 mmol) and $Ga(NO_3)_3 \cdot nH_2O$ (0.047 mmol), followed by stirring at room temperature for 1 h. The suspension was evaporated under vacuum. Subsequently, the sample was reduced with $NaBH_4$ (0.28 mmol) to yield Pd@GaO_x/CN (Pd, 1.0 wt%; Pd/Ga molar ratio = 1/1). Pd@AlO_x/CN and Pd@BO_x/CN were prepared with the same method using $Al(NO_3)_30.9\ H_2O$ and H_3BO_3, respectively. Metal loadings were determined using inductively coupled plasma (ICP) analysis. The catalysts can be synthesized with high reproducibility.

2.3. General procedure for the catalytic hydrogenation of CO_2

CO_2 hydrogenation to FA was conducted with a batch reactor system using a stainless steel autoclave (60 mL). In each trial, the catalyst (10 mg) and a 1.0-M aqueous $NaHCO_3$ solution (15 mL) were transferred into the reactor, and the pressure was set to 2.0 MPa by adding H_2 and CO_2 in a 1:1 molar ratio. The system was subsequently heated to 100 °C and stirred for 6 h. FA yields were determined with high-performance liquid chromatography at 40 °C using a Shimadzu instrument equipped with a Bio-Rad Aminex HPX-87 H ion exclusion column (300 × 7.8 mm) with 5-mM H_2SO_4 (0.5 mL/min) as the mobile phase. TON values were determined by dividing the quantity of FA produced after 6 h by the moles of total Pd or surface-exposed Pd, as appropriate.

2.4. Characterization

Powder XRD patterns were recorded using a Rigaku Ultima IV diffractometer with Cu K_α radiation (λ = 1.54056 Å). Nitrogen adsorption–desorption isotherms were acquired at − 196 °C using a BELSORP-max system (MicrotracBEL Corp.). Samples were degassed at 150 °C for 3 h under vacuum to vaporize physisorbed water prior to each trial. Specific surface areas were calculated using the BET method using nitrogen adsorption data. Metal concentrations in the samples were determined using ICP-AES analysis with a Nippon Jarrell-Ash ICAP-575 Mark II instrument. TEM images were obtained with a Hitachi H-800 instrument operating at 200 kV. STEM images and elemental maps were obtained using a JEOL-ARM 200 F apparatus equipped with a Kvex energy-dispersive X-ray detector (JED-2300 T) operating at 200 kV. CO pulse adsorption was performed by using a BEL-METAL-1 instrument (BEL Japan, Inc.) to measure the Pd dispersion. The sample was pretreated under He flow at 323 K for 15 min and subsequently under H_2 flow at 323 K for 60 min. The CO adsorption was measured at 323 K using 1%CO/He at a flow rate of 20 mL·min^{-1}. Pd and Ga K-edge XAFS spectra were recorded using a fluorescence yield collection technique with a Si(111) monochromator at the 01B1 beamline station at the SPring-8 facility, JASRI, Harima, Japan (proposal nos. 2020A0523 and 2020A1062). Data reduction was performed using the REX2000 software program (Rigaku). To obtain radial structure functions, Fourier transformation of the k^3-weighted normalized EXAFS data was carried out over the range 3.0 Å < k/Å^{-1} < 12 Å. Temperature programmed reduction with H_2 (H_2-TPR) was conducted using a BEL-CAT (BEL Japan, Inc.) instrument by heating 30 mg samples at 5 ºC min^{-1} from − 100–300 ºC under a 5.0% H_2/Ar flow. The H_2-D_2 exchange reaction was monitored using a BELCATII system (MicrotracBEL Corp.). After the pretreatment under He flow at 323 K for 30 min, the H_2-D_2 exchange reaction was performed at 323 K using 25%H_2/He and 25%D_2/He at a flow rate of 25 mL·min^{-1}. Products (H_2, HD and D_2) were analyzed with an online mass spectrometer. The rate constant was determined from the produced HD amount.

2.5. DFT calculations

All DFT calculations were performed with the DMol^3 program in the Materials Studio 17.2 software package [38,39]. The generalized gradient approximation exchange–correlation functional proposed by Perdew, Burke, and Ernzerhof was combined with the double numerical basis set plus polarization functions. A supercell slab consisting of a surface 5 × 5 unit cells with three atomic (111) surface layers was adopted. For the calculation, periodic boundary conditions were applied to the slabs. The reactant atoms and their adjacent atoms were relaxed during geometry optimizations, and the other layers were fixed at the corresponding bulk positions. Transition states (TSs) were determined using the nudged elastic band method, and the activation energy was defined by the energy difference between the TS and reactant.

3. Results and discussion

3.1. Characterization of Pd@GaO_x/CN

The deposition of metal catalysts was performed using a conventional method. Briefly, g-C_3N_4 [Brunauer–Emmett–Teller (BET) surface area S_{BET} = 7.5 m^2·g^{-1}] was impregnated with an aqueous solution of Na_2PdCl_4 and $Ga(NO_3)_3 \cdot nH_2O$. The Pd/Ga ratio in the resulting material was controlled by varying the concentration of Ga while maintaining a constant Pd loading of 1.0 wt%. The samples obtained in this manner were subsequently reduced with $NaBH_4$ without calcination, yielding Pd@GaO_x supported on g-C_3N_4 (i.e., Pd@GaO_x/CN) with various Pd/Ga atomic ratios. The same impregnation method was used to synthesize Pd@AlO_x/CN and Pd@BO_x/CN along with $Al(NO_3)_30.9\ H_2O$ and H_3BO_3 precursors as the second metals, followed by reduction with $NaBH_4$.

The X-ray diffraction (XRD) pattern of Pd@GaO_x/CN exhibited peaks due to Pd(111) and Pd(200) at 40.2° and 47.0°, respectively, with no characteristic peaks assignable to PdGa intermetallic alloy (Fig. S1). X-ray photoelectron spectroscopy (XPS) analysis showed that the peak of

the Ga 3d spectrum of Pd@GaOx/CN could be deconvoluted with the main peak centered at 20.3 eV and the minor peak centered at 19.1 eV, which reflects Ga^{3+} (95.7%) and Ga^{2+} (6.3%), respectively (Fig. S2). No peak due to metallic Ga was observed. Significant differences were not observed in the N_2 adsorption–desorption isotherms of the material before and after metal deposition ($S_{BET} = 9.7$ m$^2 \cdot$g^{-1} for Pd@GaO$_x$/CN) (Fig. S3). Pd@AlO$_x$/CN and Pd@BO$_x$/CN also showed similar S_{BET}.

The shapes of the Pd K-edge X-ray absorption near-edge structure (XANES) spectra of Pd /CN and Pd@MO$_x$/CN (M = Ga, Al, or B) differed from those of the Pd foil but resembled those of PdO with two distinct peaks attributed to the allowed 1 s–5p transition (Fig. 1a). More detailed inspection verified the differences in the shape at approximately 24,385 eV in the comparison of Pd/CN with Pd@MO$_x$/CN (M = Ga, Al, or B), indicating that the symmetry of the Pd metal face centered cubic structure was slightly disordered by integration with MO$_x$ (M = Ga, Al, or B) [18]. In the Fourier-transform extended X-ray absorption fine structure (FT-EXAFS) spectra at the Pd K-edge of each sample, the peak due to the Pd–O and/or Pd–N bond and that due to contiguous metallic Pd–Pd bonds were observed at approximately 1.6 and 2.5 Å, respectively (Fig. 1b). The first peak, at 1.6 Å, is partially due to Pd–N bonds originating from interaction with the g-C$_3$N$_4$ support. Moreover, their intensity relative to Pd–Pd bond increased in the Pd@MO$_x$/CN (M = Ga, Al, or B) compared with the monometallic Pd/CN. The inverse FT of Pd@GaO$_x$/CN was well fitted by using Pd–O and Pd–Pd shells, whose interatomic distance (R) and coordination number (CN) were determined to be $R = 2.00$ Å and CN = 4.3 and $R = 2.75$ Å and CN = 5.1, respectively (Table 1 and Fig. S4). The contribution of Pd–O bond
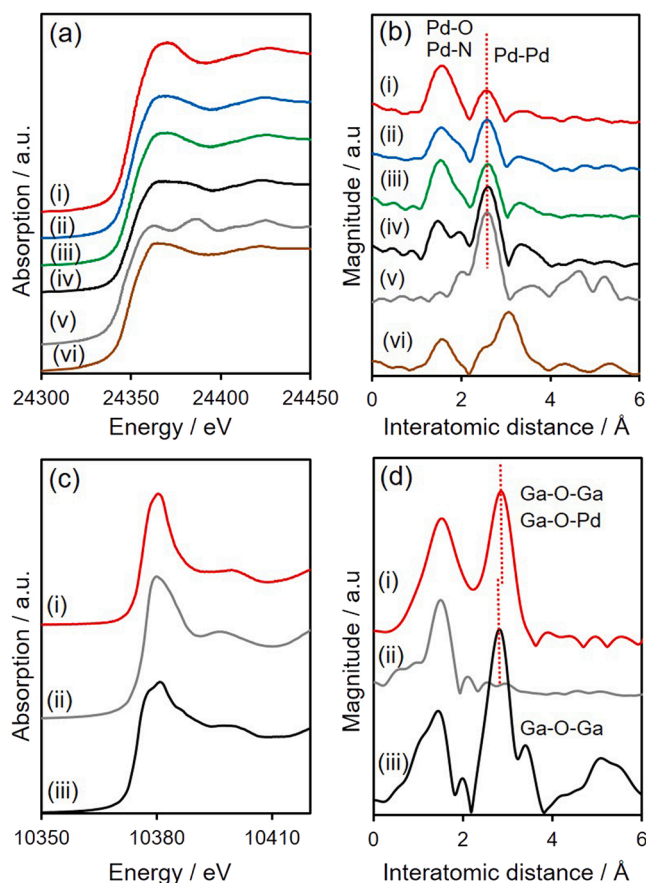

Fig. 1. (a) Pd K-edge X-ray absorption near-edge structure (XANES) and (b) Fourier-transform extended X-ray absorption fine structure (FT-EXAFS) spectra of (i) Pd@GaO$_x$/CN, (ii) Pd@AlO$_x$/CN, (iii) Pd@BO$_x$/CN, (iv) Pd/CN, (v) Pd foil, and (vi) PdO. (c) Ga K-edge XANES and (d) FT-EXAFS spectra of (i) Pd@GaO$_x$/CN, (ii) Ga(NO$_3$)$_3$, and (iii) Ga$_2$O$_3$.

Table 1
Curve fitting results determined by Pd K-edge FT-EXAFS data.

	Shell	R / Å	CN	σ^2
Pd@GaO$_x$/CN	Pd-O	2.00	5.1	0.0069
	Pd-Pd	2.75	5.0	0.0096
Pd@AlO$_x$/CN	Pd-O	2.01	3.3	0.00660
	Pd-Pd	2.76	5.2	0.0086
Pd@BO$_x$/CN	Pd-O	2.01	3.1	0.0046
	Pd-Pd	2.76	4.8	0.0055
Pd/CN	Pd-O	2.01	2.5	0.0055
	Pd-Pd	2.76	5.8	0.0076

increased in the order of Pd@GaO$_x$/CN > Pd@AlO$_x$/CN ≈ Pd@BO$_x$/CN > Pd$_x$/CN. These results suggest that the surfaces of Pd NPs are oxidized by modification with MO$_x$ to some extent. As will be discussed later, curve-fitting results are consistent with the those obtained from CO adsorption, in which the exposed Pd dispersion decreased in the order of Pd@GaO$_x$/CN < Pd@AlO$_x$/CN ≈ Pd@BO$_x$/CN < Pd$_x$/CN. No shift of the second Pd–Pd bond was observed for all samples compared with Pd, which may rule out the formation of intermetallic alloy compounds.

The shape of the Ga K-edge XANES spectrum of Pd@GaO$_x$/CN was intermediate between that of Ga(NO$_3$)$_3 \cdot n$H$_2$O and Ga$_2$O$_3$ (Fig. 1c). The FT-EXAFS spectrum of Pd@GaO$_x$/CN exhibited two peaks at approximately 1.6 and 2.5 Å due to the Ga–O bond and Ga–O–Ga bond, respectively (Fig. 1d). The intensity of the second peak in the spectrum of Pd@GaO$_x$/CN was slightly weaker than that in the reference spectrum of Ga$_2$O$_3$. The reduced intensity in this region can be explained by the formation of structurally disordered NPs of extremely small size [40]. Additionally, the Ga–O–Ga bond in the spectrum of Pd@GaO$_x$/CN was slightly shifted to a longer interatomic distance than that of Ga$_2$O$_3$, which is indicative of the formation of Ga–O–Pd bond. No metallic bonds were observed. Because the reduction potentials of Ga^{3+} ions [E° (Ga^{3+}/Ga^{2+}) = −0.59 V vs. the normal hydrogen electrode (NHE)] are more negative than those of Pd^{2+} ions [E° (Pd^{2+}/Pd^0) = +0.99 V vs. NHE], the reduction of Ga^{3+} ions was delayed more than that of Pd^{2+} ions, leading to preferential formation of amorphous MO$_x$ phase on the surface of Pd NPs via Pd–O–Ga bonds.

In the temperature-programmed reduction under hydrogen (H$_2$-TPR). The peak attributed to the reduction of PdO to metallic Pd observed in Pd/CN was broadened and shifted to a higher temperature in Pd@GaO$_x$/CN (Fig. S5). This indicates that the GaO$_x$ phase exists in the periphery of the Pd NPs, which influences the reduction sequence of Pd NPs. A high-angle annular dark-field scanning transmission electron microscopy (STEM) image of Pd@GaO$_x$/CN is shown in Fig. 2a. Energy-dispersive X-ray spectroscopy maps of a selected area demonstrate that the white particle is composed of Pd and that the Ga atoms are highly dispersed throughout the material (Fig. 2b and c). The mean particle diameter (d_{ave}) was determined to be 6.3 nm (Fig. 2d). This value is comparable with that obtained for Pd/CN ($d_{ave} = 5.3$ nm), Pd@AlO$_x$/CN ($d_{ave} = 6.5$ nm), and Pd@BO$_x$/CN ($d_{ave} = 6.8$ nm), as summarized in Fig. S6. The elemental distribution across the surface of a single NP provided strong evidence that Ga atoms occur in the periphery of Pd NPs (Fig. 2e). More detailed investigation suggests that Pd NPs exposed Pd (111) with a D-spacing of 0.224 nm (Fig. 2f and g), while no crystal phase was observed in its periphery despite Ga atoms being confirmed by EDX (Fig. 2h). By considering these results as well as the differences in reduction potential between Pd^{2+} and Ga^{3+}, a possible structure was proposed, in which amorphous GaO$_x$ phases were partially located on the surfaces of Pd NPs, as illustrated in Fig. 2i.

In an effort to investigate the influence of GaO$_x$ phase on the electronic state of the active Pd species, atomic charges were calculated using DFT. Here we considered supercell slab models consisting of a surface 5 × 5 surface unit cells including Pd(111) interacting with a M$_2$O$_3$ cluster (M = Ga, Al, or B). The optimized structure of Pd(111) associated with a single stoichiometric Ga$_2$O$_3$ cluster is shown in Fig. 3A (a). The colors of Pd atoms in this figure refer to their calculated
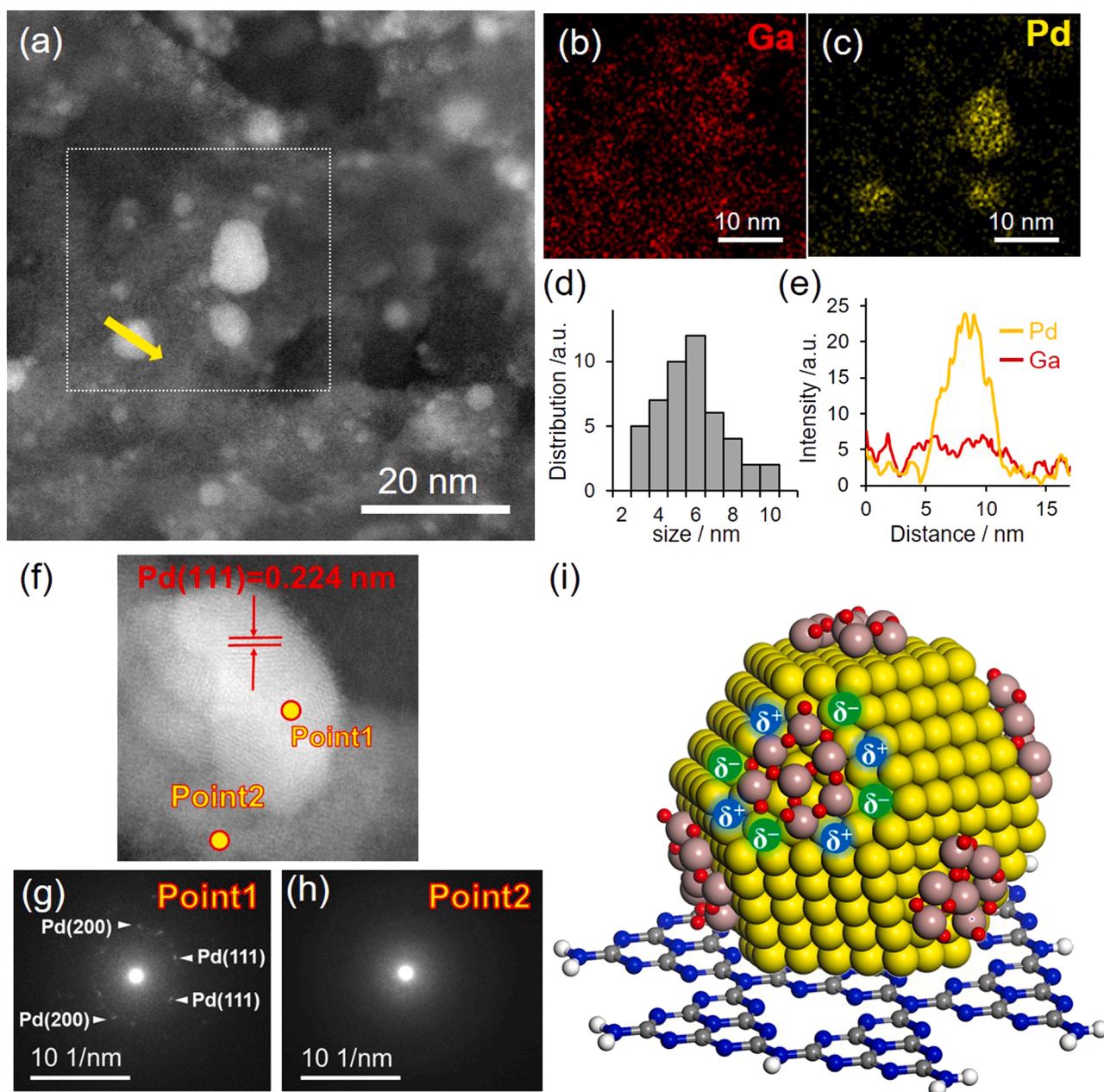
Fig. 2. (a) A HAADF-STEM image of Pd@GaO$_x$/CN. (b, c) EDS maps for (b) Ga and (c) Pd. (d) Size distribution of nanoparticles determined from STEM image. (e) Cross-sectional EDS line profile obtained from a single nanoparticle in Fig. 2a. (f) HAADF-STEM image in the other area, (g, h) electron diffraction patters of Point 1 and point 2 in (f). (i) Structural model of Pd@GaO$_x$/CN.

Mulliken atomic charges. This analysis demonstrated that an electron is transferred from the Ga atom of Ga$_2$O$_3$ to a nearby Pd atom. The four green Pd atoms in the periphery of the Ga atom were strongly negatively charged. In contrast, the blue Pd atoms bounded by the O atoms of Ga$_2$O$_3$ were positively charged, indicating electron transfer from the Pd atoms to the O atoms. Such electronic interaction generates the unique Pd ensemble sites where electron-deficient Pd$^{\delta+}$ and electron-rich Pd$^{\delta-}$ are adjacent. A similar tendency can be observed in the case of Pd(111) associated with one stoichiometric Al$_2$O$_3$ (Fig. 3A(b)) or B$_2$O$_3$ (Fig. 3A (c)) cluster; the Pd atoms in the vicinity of the B atom were negatively charged, whereas the Pd atoms connected with the O atoms were positively charged. However, the degrees of positivity and negativity observed in the presence of the B$_2$O$_3$ cluster were smaller than those observed in the presence of the Ga$_2$O$_3$ or Al$_2$O$_3$ cluster. This phenomenon can be explained by the small electronegativities of Ga (1.81) and Al

(1.61) compared with those of B (2.04), causing electron transfer from Ga or Al to Pd (2.20) to be better facilitated than that from B. In the preliminary calculation of Density of State (DOS) values, d-band center of Pd(111) + Ga$_2$O$_3$ was found to be located at − 2.05 eV, which is almost similar to the value of − 2.01 eV for Pd (111) (Fig. 3B). This indicates that GaO$_x$ modification does not ameliorate the electronic structure in the bulk, but causes uneven charge distribution on their surface. These results were further evidenced by XPS spectra. The shift of the Pd 3d peaks generated by Pd@GaO$_x$/CN to lower binding energy was limited to only 0.15 eV compared with that obtained from the monometallic Pd/CN (Fig. S7), presumably because the uneven charge distribution at the quite limited area (adjacent electron-deficient Pd$^{\delta+}$ and electron-rich Pd$^{\delta-}$) is averaged and is not reflected in XPS spectra.
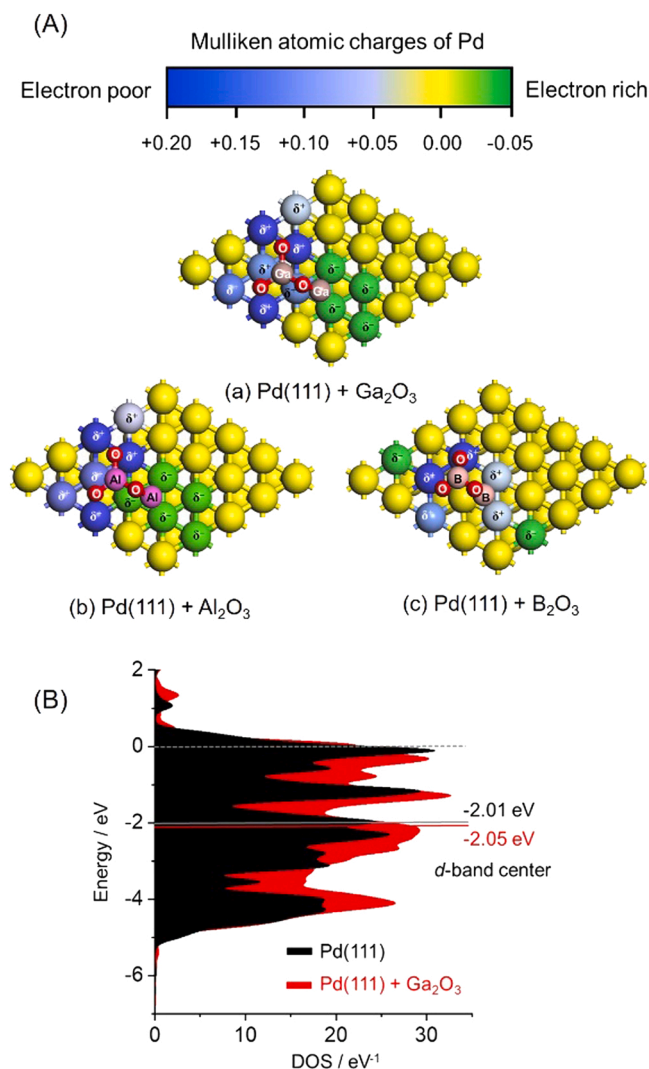
Fig. 3. (A) The optimized structure of Pd(111) associated with one stoichiometric cluster of (a) Ga_2O_3, (b) Al_2O_3, and (c) B_2O_3 with a color overlay of representative Mulliken atomic charge determined using density functional theory calculations. (B) Calculated DOS plots.

3.2. Catalytic and mechanistic investigation of CO_2 hydrogenation

Catalytic activity in CO_2 hydrogenation to formate was examined using a series of Pd-based catalysts, with results shown in Fig. 4a. A typical reaction was performed in a basic aqueous solution containing 1.0 M $NaHCO_3$ under a total pressure of 2.0 MPa (H_2:CO_2 = 1:1) at 100 °C over 6 h. Comparing the TON values based on the total quantities of Pd employed, Pd@MO$_x$/CN (M = Ga, Al, or B) exhibited a TON value comparable with or higher than that of monometallic Pd/CN despite the low density of surface-exposed Pd atoms on Pd@MO$_x$/CN, in which activity increased in the order of Pd@GaO$_x$/CN < Pd@AlO$_x$/CN < Pd@BO$_x$/CN. In an effort to elucidate the potential activity, the dispersion of Pd species was determined using pulsed CO adsorption measurements (Table S1). Since the exposed Pd dispersion of Pd@GaOx/CN is only 6.5%, a maximum TON value of 4540 (yield of FA = 0.012 mol·h^{-1}·g$_{cat}^{-1}$) was obtained for Pd@GaO$_x$/CN based on the quantity of surface-exposed Pd atoms, representing a more than sixfold increase compared with monometallic Pd/CN. FA was obtained with > 99% selectivity and any other products were not observed. The catalytic activity is comparable to and better than some of the previously reported systems (Table S2). The differences in MOx coverage may be attributed to the affinity between the Pd and a group 13 element. No other byproducts were found in either liquid or gas phase for any catalyst employed. Notably, Pd/Ga_2O_3 prepared using the same impregnation method, followed by $NaBH_4$ reduction, showed almost no catalytic activity, indicating that Ga_2O_3 itself does not act as an efficient support. The composition of the Pd@GaO$_x$/CN catalyst was tuned simply by varying the initial molar ratio of the metal precursors. The effect of Ga content on the TON based on the quantity of surface-exposed Pd atoms is shown in Fig. 4b, in which activity was maximized atGa = 40 at %. Such precipitously peaked activity order based on the Pd/Ga composition clearly suggests that the synergistic effect originated from the integration of Pd with Ga and that the excess GaO$_x$ may suppress the ease of access to the active Pd centers.

Furthermore, the CO_2 hydrogenation reaction under additive-free aqueous conditions (CO_2 (aq.) + H_2 (aq.) → HCOOH (aq.), ΔG = -4 kJ mol$-$ 1) is recently highly desired from an industrial perspective. The Pd@GaOx/CN displayed high activity (TON=59 at 24 h, TOF=2.5 h^{-1}) in the FA production under additive-free aqueous conditions (that is, in distilled water) with a total pressure of 4.0 MPa (H_2/CO_2 =1:1) at 40 °C. The attained activity is comparable to and better than some of the previously reported systems, such as PdNi/carbon nanotube (TOF = 0.2 h^{-1}) [8], Pd/g-C_3N_4 (1.5 h^{-1}) [41], and Pd/C_3N_4 with edge defect (TOF =2.4 h^{-1}) [42], respectively.

A possible reaction mechanism for CO_2 hydrogenation to formate over supported metal NPs, taking into account previous studies, is proposed in Fig. 5a [43–45]. First, the dissociation of H_2 is initiated, yielding a metal hydride species (*step 1*). This is followed by the adsorption of HCO_3^-, which is transformed from gaseous CO_2 under basic aqueous solutions (*step 2*). Next, dissociated active H atoms attack C atoms of adsorbed HCO_3^- ions to give a formate intermediate (*step 3*). The reduction of HCO_3^- is energetically more likely to proceed by the attack of active H on the C atom rather than on the O atoms. Finally, the O atom of the OH group undergoes attack by another H atom (*step 4*), leading to the production of formate and H_2O (*step 5*), regenerating the initial active species.

In the reaction under a flow of H_2 and D_2 through the catalyst, the formation rate of HD was significantly enhanced by Pd@MO$_x$/CN (M = Ga, Al, or B) compared with Pd/CN, and Pd@GaO$_x$/CN was the most active among the investigated systems, as shown in Fig. 4c. This finding is consistent with the order of catalytic activity in CO_2 hydrogenation. This alignment demonstrates that the addition of group 13 elements promotes dissociation of hydrogen on NP surfaces (*step 1*) [46].

Moreover, the effect of HCO_3^- concentration was also critically dependent on the catalyst composition (Fig. 4d–g). All Pd@MO$_x$/CN catalysts displayed higher reaction orders (Ga, 0.71; Al, 0.74; B, 0.67) than Pd/CN (0.60), as determined using the slope obtained at low HCO_3^- concentration. This means the HCO_3^- adsorption step is enhanced by interfacial modification. It should be further noted that Pd@GaO$_x$/CN showed a linear relationship between TON and the HCO_3^- concentration across the full range of values. Activity increases with increasing HCO_3^- concentration without saturation because the subsequent reaction of the adsorbed HCO_3^- species (*step 3*) occurs smoothly over Pd@GaO$_x$/CN. In contrast, TON values were almost constant across high HCO_3^- concentrations for each of the other catalysts. These results suggest that the adsorption sites over such catalysts are likely to be saturated because of the delay of the subsequent reaction of the adsorbed HCO_3^- species.

To better understand the positive effect of interfacial MO$_x$ (M = Ga, Al, or B) modification, potential energy profiles were calculated, employing Pd(111) slab models interacting with a M_2O_3 cluster (M = Ga, Al, or B) (Fig. 5b). In the case of Pd(111), H_2 dissociation at Pd sites (*step 1*) is initiated with an activation energy (E_a) of 23.8 kcal·mol^{-1}. Next, HCO_3^- is adsorbed on Pd to produce intermediate III (*step 2*), with an adsorption energy (E_{ad}) determined to be -57.9 kcal·mol^{-1}. Then, reduction takes place through the attack of a hydride ion with an energy barrier of 67.4 kcal·mol^{-1} (*step 3*). The energy barrier is negligibly small in *step 4*, in which formate is spontaneously generated along with H_2O when the OH of HCO_3^- is attacked by another hydride ion. These results
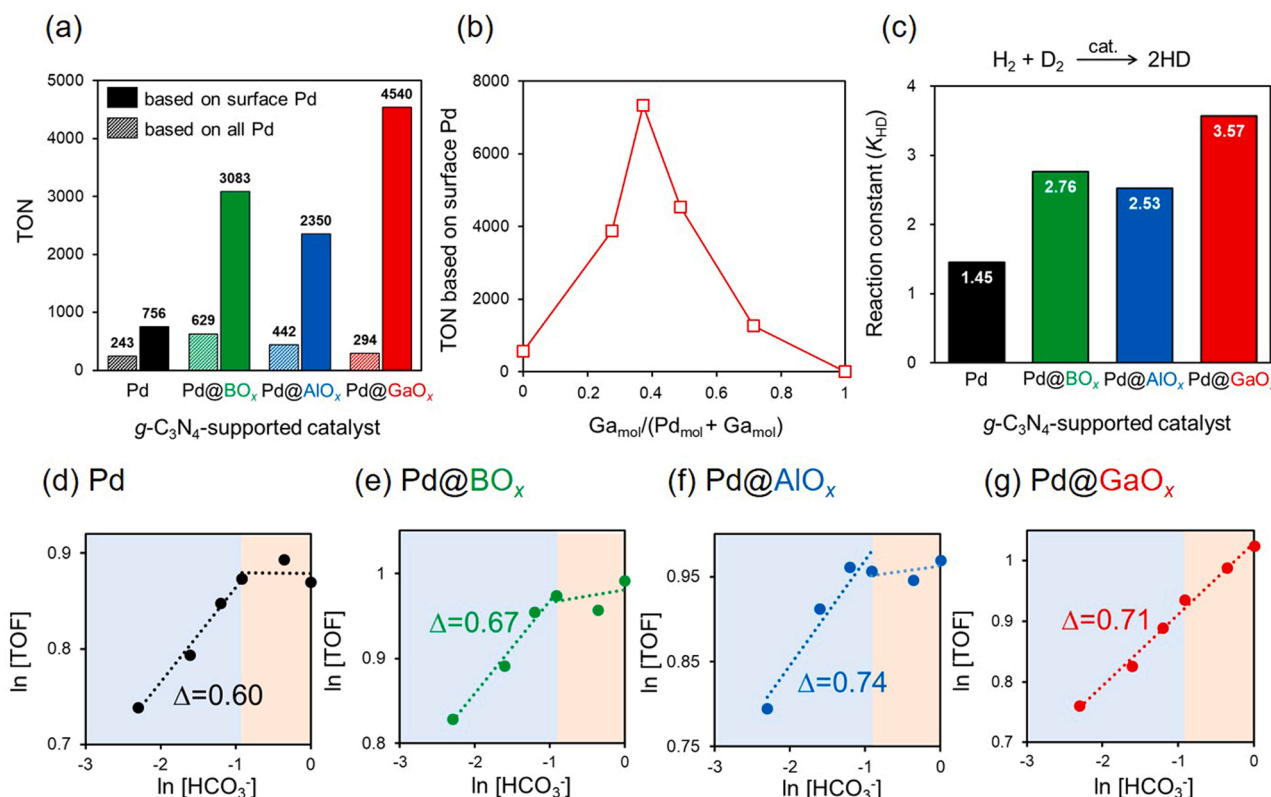
Fig. 4. (a) Comparison of catalytic activity for a series of supported Pd-based catalysts during CO_2 hydrogenation. (b) TON values based on surface Pd atoms versus the atomic fraction of Ga for Pd@GaO$_x$/CN catalysts of various Pd and Ga concentrations. (c) Comparison of activity during the HD exchange reaction for a series of supported Pd-based catalysts. (d–g) Effect of HCO_3^- concentration on TOF values for a series of supported Pd-based catalysts: (d) Pd, (e) Pd@BO$_x$/CN, (f), Pd@AlO$_x$/CN, and (g) Pd@GaO$_x$/CN.

revealed that the rate-determining step in the present catalytic cycle is *step 3*. This is consistent with insights obtained from our previous experimental and theoretical studies [15,16].

In the case of Pd(111) associated with Ga_2O_3, the dissociation of H_2 occurs with an energy barrier of 13.0 kcal·mol^{-1}, which is lower than that obtained for Pd(111) alone. This result agrees with the kinetic data obtained for the HD formation reaction (Fig. 4c). Similarly, the presence of Al_2O_3 and B_2O_3 slightly lowered the E_a for H_2 dissociation, as also verified in the kinetic investigations. As discussed above (Fig. 3a), there is an electron transfer from the Ga atoms of Ga_2O_3 to the Pd atoms. This process generates the electron-rich Pd$^{\delta-}$, which facilitates the dissociation of H_2 because the H_2 activation process requires the electron to be injected into the H 1 s antibonding state [47].

The E_{ad} values of HCO_3^- in *step 2* for Pd(111) interacting with the M_2O_3 cluster (M = Ga, Al, or B) increased in the following order: B (−63.9 kcal·mol^{-1}) < Al (−67.9 kcal·mol^{-1}) < Ga (−72.5 kcal·mol^{-1}). As expected, these values were higher than those for adsorption on pristine Pd(111) (E_{ad} = −57.9 kcal·mol^{-1}). This calculation result is in agreement with the effect of HCO_3^- concentration on catalytic activity, for which Pd@MO$_x$/CN catalysts displayed reaction orders higher than those of Pd/CN (Fig. 4d–g). Thus, interfacial modification with group 13 elements plays an important role in the stabilization of HCO_3^- ions; in comparison with the situation in pristine Pd(111), the Mulliken atomic charges of Pd atoms bounded by O atoms of M_2O_3 were positively charged by electron transfer from the Pd atoms to the O atoms, and the degrees of positivity and negativity were larger in Ga_2O_3 (Fig. 3). The generation of such electron-deficient Pd$^{\delta+}$ accordingly increased the adsorption of HCO_3^-. This increase further promoted the subsequent reduction of HCO_3^- (*step 4*), since the larger E_{ad} for the reaction intermediate on the metal catalyst corresponded to a lower reaction barrier according to the Brønsted–Evans–Polanyi relationship [48].

As expected, the E_a for the reduction of HCO_3^- for Pd(111) interacting with a M_2O_3 cluster (M = Ga, Al, or B) was lower than that for pristine Pd (111), and more significant enhancement of this step was observed for Pd(111) interacting with a M_2O_3 cluster than for pristine Pd(111). These results are also in good agreement with our kinetic investigation into the effect of HCO_3^- concentration. In that context, the catalytic activity increased with increasing HCO_3^- concentration without saturation even at high concentrations. These results further demonstrate that modification with group 13 elements plays a pivotal role in boosting performance at the rate-determining step.

The enhancement in the rate-determining step can be explained by considering the electronic state in reaction intermediate III in Fig. 5a. DFT-optimized configurations are summarized in Fig. 6. The C atoms of the adsorbed HCO_3^- ions at an electron-deficient Pd$^{\delta+}$ site over Pd(111) interacting with a Ga_2O_3 cluster are more positively charged than elsewhere, as shown in Table 1. In contrast, the electronic charges of the dissociated hydride species at an electron-rich Pd$^{\delta-}$ site are negative. Therefore, the more strongly positive C atoms of the adsorbed HCO_3^- ions are the most likely carbon atoms to undergo attack by the dissociated hydride species. It can thus be concluded that the electronic effect resulting from the interplay of the Pd ensemble sites induced by GaO$_x$ modification explains the enhanced activity during CO_2 hydrogenation. With respect to the above-mentioned mechanism, we also point out the participation of multiple interactions at the metal/support interface [49, 50]. The interaction of HCO_3^- with *g*-C_3N_4 support via the formation of O–H···N hydrogen bonds give rise to the positively polarized carbon in HCO_3^-, which easily undergoes the attacks by the dissociated H atom at Pd accompanied by the simultaneous formation of the formate intermediate. The electron density transfer from the semiconductor *g*-C_3N_4 to Pd NPs in the heterojunction also plays an important role in the formation of electronically enriched metallic Pd [49] Table 2.
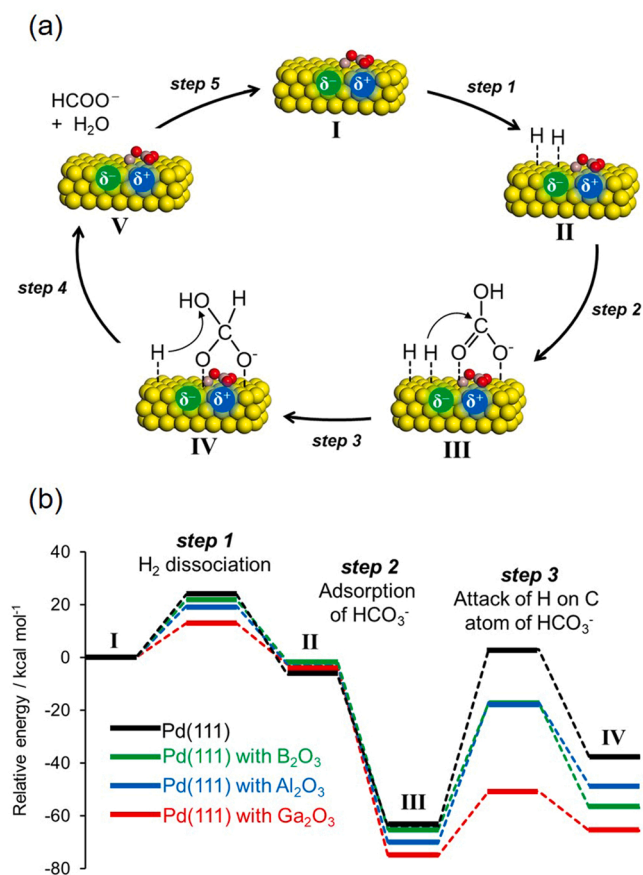
Fig. 5. (a) Possible reaction mechanism for the hydrogenation of CO_2 to formate and (b) the corresponding potential energy profiles as determined using density functional theory calculations for Pd (111) and Pd(111) associated with a M_2O_3 cluster (M = Ga, Al, or B).
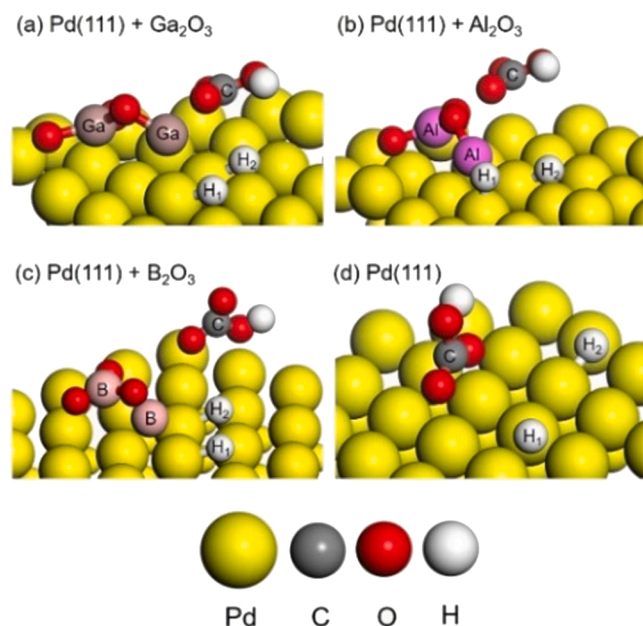

Fig. 6. DFT-optimized configurations for dissociated H atoms and HCO_3^- ions adsorbed on (a, b, and c) PdAg (111) associated with an M_2O_3 (M = Ga, Al, or B) and (d) PdAg (111).

Table 2
Adsorption energy values (E_{ad}) for HCO_3^- and representative Mulliken atomic charges as determined using density functional theory calculations involving the reaction intermediates in the rate-determining steps for bare Pd(111) and Pd (111) associated with the M_2O_3 cluster (M = Ga, Al, or B).

Sample	E_{ad} of HCO_3^- (kcal·mol^{-1})	Atomic charge		
		C atom of HCO_3^-	H atom	
			H_1	H_2
Pd(111) + Ga$_2$O$_3$	− 72.5	0.734	− 0.029	− 0.003
Pd(111) + Al$_2$O$_3$	− 67.9	0.675	− 0.006	− 0.059
Pd(111) + B$_2$O$_3$	− 63.9	0.666	0.002	− 0.019
Pd(111)	− 57.9	0668	− 0.031	− 0.018

4. Conclusions

We successfully achieved enhanced activity of a Pd-based catalyst during CO_2 hydrogenation to FA via interfacial modification with highly dispersed amorphous MO_x phase (M = Ga, Al, or B). In particular, the activity of Pd@GaO$_x$/CN was enhanced sixfold relative to that of monometallic Pd/CN based on the quantity of surface-exposed Pd atoms. Dual activation of hydrogen and HCO_3^- over ensemble Pd sites was elucidated by kinetics data and DFT calculations. The electron-deficient Pd$^{\delta+}$ species associated with O atoms of Ga$_2$O$_3$ enhanced the adsorption energy of HCO_3^- ions, whereas the electron-rich Pd$^{\delta-}$ species in the periphery of the Ga atom promoted H_2 dissociation as well as the attack of dissociated H atoms on C atoms in HCO_3^- ions. This study thus provides key information on the advanced design of catalytic active centers for CO_2 hydrogenation to FA. The findings also emphasize the importance of interface design for further improvement of catalytic performance, resulting in a key practical application: the realization of a reversible, environmentally friendly hydrogen storage system mediated by CO_2 and FA.

CRediT authorship contribution statement

Kohsuke Mori: Conceptualization, Supervision, Writing – original draft preparation, Validation. **Hiroto HATA:** Visualization, Investigation, Validation. **Hiromi Yamashita:** Supervision.

Declaration of Competing Interest

The authors declare that they have no known competing financial interests or personal relationships that could have appeared to influence the work reported in this paper.

Data Availability

No data was used for the research described in the article.

Appendix A. Supporting information

Supplementary data associated with this article can be found in the online version at doi:10.1016/j.apcatb.2022.122022.

References

[1] E.V. Kondratenko, G. Mul, J. Baltrusaitis, G.O. Larrazabal, J. Perez-Ramirez, Status and perspectives of CO_2 conversion into fuels and chemicals by catalytic, photocatalytic and electrocatalytic processes, Energy Environ. Sci. 6 (2013) 3112–3135.

[2] P.G. Jessop, T. Ikariya, R. Noyori, Homogeneous hydrogenation of carbon dioxide, Chem. Rev. 95 (1995) 259–272.

[3] S. Enthaler, Carbon dioxide—the hydrogen-storage material of the future? ChemSusChem 1 (2008) 801–804.

[4] S. Enthaler, J. von Langermann, T. Schmidt, Carbon dioxide and formic acid-the couple for environmental-friendly hydrogen storage? Energy Environ. Sci. 3 (2010) 1207–1217.

[5] P. Verma, S. Zhang, S. Song, K. Mori, Y. Kuwahara, M. Wen, H. Yamashita, T. An, Recent strategies for enhancing the catalytic activity of CO_2 hydrogenation to formate/formic acid over Pd-based catalyst, J. CO_2 Util. 54 (2021), 101765.

[6] S. Moret, P.J. Dyson, G. Laurenczy, Direct synthesis of formic acid from carbon dioxide by hydrogenation in acidic media, Nat. Commun. 5 (2014) 4017.

[7] P.G. Jessop, F. Joó, C.-C. Tai, Recent advances in the homogeneous hydrogenation of carbon dioxide, Coord. Chem. Rev. 248 (2004) 2425–2442.

[8] L.T.M. Nguyen, H. Park, M. Banu, J.Y. Kim, D.H. Youn, G. Magesh, W.Y. Kim, J. S. Lee, Catalytic CO_2 hydrogenation to formic acid over carbon nanotube-graphene supported PdNi alloy catalysts, RSC Adv. 5 (2015) 105560–105566.

[9] D. Mellmann, P. Sponholz, H. Junge, M. Beller, Formic acid as a hydrogen storage material - development of homogeneous catalysts for selective hydrogen release, Chem. Soc. Rev. 45 (2016) 3954–3988.

[10] K. Sordakis, C. Tang, L.K. Vogt, H. Junge, P.J. Dyson, M. Beller, G. Laurenczy, Homogeneous catalysis for sustainable hydrogen storage in formic acid and alcohols, Chem. Rev. 118 (2018) 372–433.

[11] D. Mellmann, P. Sponholz, H. Junge, M. Beller, Formic acid as a hydrogen storage material – development of homogeneous catalysts for selective hydrogen release, Chem. Soc. Rev. 45 (2016) 3954–3988.

[12] A. Álvarez, A. Bansode, A. Urakawa, A.V. Bavykina, T.A. Wezendonk, M. Makkee, J. Gascon, F. Kapteijn, Challenges in the greener production of formates/formic acid, methanol, and DME by heterogeneously catalyzed CO_2 hydrogenation processes, Chem. Rev. 117 (2017) 9804–9838.

[13] K. Mori, T. Taga, H. Yamashita, Isolated single-atomic Ru catalyst bound on a layered double hydroxide for hydrogenation of CO_2 to formic acid, ACS Catal. 7 (2017) 3147–3151.

[14] G.H. Gunasekar, K. Park, K.-D. Jung, S. Yoon, Recent developments in the catalytic hydrogenation of CO_2 to formic acid/formate using heterogeneous catalysts, Inorg. Chem. Front. 3 (2016) 882–895.

[15] K. Mori, T. Sano, H. Kobayashi, H. Yamashita, Surface engineering of a supported PdAg catalyst for hydrogenation of CO_2 to formic acid: elucidating the active Pd atoms in alloy nanoparticles, J. Am. Chem. Soc. 140 (2018) 8902–8909.

[16] K. Mori, A. Konishi, H. Yamashita, Interfacial engineering of PdAg/TiO_2 with a metal–organic framework to promote the hydrogenation of CO_2 to formic acid, J. Phys. Chem. C. 124 (2020) 11499–11505.

[17] K. Mori, H. Yamashita, Progress in design and architecture of metal nanoparticles for catalytic applications, Phys. Chem. Chem. Phys. 12 (2010) 14420–14432.

[18] K. Mori, N. Hashimoto, N. Kamiuchi, H. Yoshida, H. Kobayashi, H. Yamashita, Hydrogen spillover-driven synthesis of high-entropy alloy nanoparticles as a robust catalyst for CO_2 hydrogenation, Nat. Commun. 12 (2021) 3884.

[19] C. Xie, Z. Niu, D. Kim, M. Li, P. Yang, Surface and interface control in nanoparticle catalysis, Chem. Rev. 120 (2020) 1184–1249.

[20] P. Paalanen, B.M. Weckhuysen, M. Sankar, Progress in controlling the size, composition and nanostructure of supported gold–palladium nanoparticles for catalytic applications, Catal. Sci. Tech. 3 (2013) 2869–2880.

[21] K. Mori, T. Hara, T. Mizugaki, K. Ebitani, K. Kaneda, Hydroxyapatite-supported palladium nanoclusters: a highly active heterogeneous catalyst for selective oxidation of alcohols by use of molecular oxygen, J. Am. Chem. Soc. 126 (2004) 10657–10666.

[22] Q. Zhang, W. Deng, Y. Wang, Effect of size of catalytically active phases in the dehydrogenation of alcohols and the challenging selective oxidation of hydrocarbons, Chem. Commun. 47 (2011) 9275–9292.

[23] B. Roldan Cuenya, Metal nanoparticle catalysts beginning to shape-up, Acc. Chem. Res. 46 (2013) 1682–1691.

[24] Z. Li, S. Ji, Y. Liu, X. Cao, S. Tian, Y. Chen, Z. Niu, Y. Li, Well-defined materials for heterogeneous catalysis: from nanoparticles to isolated single-atom sites, Chem. Rev. 120 (2020) 623–682.

[25] R. Rizo, B. Roldan Cuenya, Shape-controlled nanoparticles as anodic catalysts in low-temperature fuel cells, ACS Energy Lett. 4 (2019) 1484–1495.

[26] L. Wang, L. Wang, X. Meng, F.-S. Xiao, New strategies for the preparation of sinter-resistant metal-nanoparticle-based catalysts, Adv. Mater. 31 (2019) 1901905.

[27] X. Qian, Y. Kuwahara, K. Mori, H. Yamashita, Silver nanoparticles supported on CeO₂-SBA-15 by microwave irradiation possess metal–support interactions and enhanced catalytic activity, Chem. Eur. J. 20 (2014) 15746–15752.

[28] H. Wang, L. Wang, D. Lin, X. Feng, Y. Niu, B. Zhang, F.-S. Xiao, Strong metal–support interactions on gold nanoparticle catalysts achieved through Le Chatelier's principle, Nat. Catal. 4 (2021) 418–424.

[29] L.M. Rossi, J.L. Fiorio, M.A.S. Garcia, C.P. Ferraz, The role and fate of capping ligands in colloidally prepared metal nanoparticle catalysts, Dalton Trans. 47 (2018) 5889–5915.

[30] T. Yoshii, D. Umemoto, Y. Kuwahara, K. Mori, H. Yamashita, Engineering of surface environment of pd nanoparticle catalysts on carbon support with pyrene–thiol ligands for semihydrogenation of alkynes, ACS Appl. Mater. Interfaces 11 (2019) 37708–37719.

[31] S. Li, W. Tian, Y. Liu, The ligand effect of atomically precise gold nanoclusters in tailoring catalytic properties, Nanoscale 13 (2021) 16847–16859.

[32] Z.B. Shifrina, V.G. Matveeva, L.M. Bronstein, Role of polymer structures in catalysis by transition metal and metal oxide nanoparticle composites, Chem. Rev. 120 (2020) 1350–1396.

[33] I. NotarFrancesco, F. Fontaine-Vive, S. Antoniotti, Synergy in the catalytic activity of bimetallic nanoparticles and new synthetic methods for the preparation of fine chemicals, ChemCatChem 6 (2014) 2784–2791.

[34] K. Kusada, H. Kitagawa, A route for phase control in metal nanoparticles: a potential strategy to create advanced materials, Adv. Mater. 28 (2016) 1129–1142.

[35] K. Kusada, D. Wu, H. Kitagawa, Metal-based solid-solution alloy nanoparticles: binary to high-entropy alloys (New Aspects of Platinum Group), Chem. Eur. J. 26 (2020) 5105–5130.

[36] S. Masuda, K. Shun, K. Mori, Y. Kuwahara, H. Yamashita, Synthesis of a binary alloy nanoparticle catalyst with an immiscible combination of Rh and Cu assisted by hydrogen spillover on a TiO_2 support, Chem. Sci. 11 (2020) 4194–4203.

[37] K. Mori, D. Tatsumi, T. Iwamoto, Y. Masui, M. Onaka, H. Yamashita, Ruthenium (II)−Bipyridine/C_3N_4 hybrids: tunable photochemical properties by using exchangeable alkali metal cations, Chem. Asian J. 13 (2018) 1348–1356.

[38] B. Delley, An All-Electron, Numerical method for solving the local density functional for polyatomic molecules, J. Chem. Phys. 92 (1990) 508–517.

[39] B. Delley, From molecules to solids with the DMol³ approach, J. Chem. Phys. 113 (2000) 7756–7764.

[40] S.-T. Wong, J.-F. Lee, S. Cheng, C.-Y. Mou, In-situ study of MCM-41-supported iron oxide catalysts by XANES and EXAFS, Appl. Catal. A Gen. 198 (2000) 115–126.

[41] H. Park, J.H. Lee, E.H. Kim, K.Y. Kim, Y.H. Choi, D.H. Youn, J.S. Lee, A highly active and stable palladium catalyst on a g-C_3N_4 support for direct formic acid synthesis under neutral conditions, Chem. Commun. 52 (2016) 14302–14305.

[42] C. Mondelli, B. Puértolas, M. Ackermann, Z. Chen, J. Pérez-Ramírez, Enhanced base-free formic acid production from CO_2 on Pd/g-C_3N_4 by tuning of the carrier defects, ChemSusChem 11 (2018) 2859–2869.

[43] G.A. Filonenko, W.L. Vrijburg, E.J.M. Hensen, E.A. Pidko, On the activity of supported au catalysts in the liquid phase hydrogenation of CO_2 to formates, J. Catal. 343 (2016) 97–105.

[44] S. Masuda, K. Mori, Y. Futamura, H. Yamashita, PdAg nanoparticles supported on functionalized mesoporous carbon: promotional effect of surface amine groups in reversible hydrogen delivery/storage mediated by formic Acid/CO_2, ACS Catal. 8 (2018) 2277–2285.

[45] C.-S. He, L. Gong, J. Zhang, P.-P. He, Y. Mu, Highly selective hydrogenation of CO_2 into formic acid on a nano-Ni catalyst at ambient temperature: process, mechanisms and catalyst stability, J. CO_2 Util. 19 (2017) 157–164.

[46] L. Bai, X. Wang, Q. Chen, Y. Ye, H. Zheng, J. Guo, Y. Yin, C. Gao, Explaining the size dependence in platinum-nanoparticle-catalyzed hydrogenation reactions, Angew. Chem. Int. Ed. 55 (2016) 15656–15661.

[47] Z. Wei, J. Wang, S. Mao, D. Su, H. Jin, Y. Wang, F. Xu, H. Li, Y. Wang, In situ-generated Co0-Co3O4/N-doped carbon nanotubes hybrids as efficient and chemoselective catalysts for hydrogenation of nitroarenes, ACS Catal. 5 (2015) 4783–4789.

[48] M. Tang, J. Deng, M. Li, X. Li, H. Li, Z. Chen, Y. Wang, 3d-Interconnected hierarchical porous N-doped carbon supported ruthenium nanoparticles as an efficient catalyst for toluene and quinoline hydrogenation, Green Chem. 18 (2016) 6082–6090.

[49] X. Shao, X. Xu, Y. Huang, X. Su, H. Duan, X. Wang, T. Zhang, Pd@C3N4 nanocatalyst for highly efficient hydrogen storage system based on potassium bicarbonate/formate, AIChE J. 62 (2016) 2410–2418.

[50] J.H. Lee, J. Ryu, J.Y. Kim, S.-W. Nam, J.H. Han, T.-H. Lim, S. Gautam, K.H. Chae, C.W. Yoon, Carbon dioxide mediated, reversible chemical hydrogen storage using a Pd nanocatalyst supported on mesoporous graphitic carbon nitride, J. Mater. Chem. A 2 (2014) 9490–9495.